

# Divalent Ion Pillaring and Coating on Lithium Cobalt Oxide Cathode for Fast Intercalation of $\text{Li}^+$ Ion with High Capacity

Fuead Hasan,\* Ahmed Adel A. Abdelazeez, Mohamed Rabia, and Hyun Deog Yoo\*

The development of high-performance lithium-ion batteries (LIBs) is essential for sustainable energy storage and utilization. Lithium cobalt oxide ( $\text{LiCoO}_2$ , LCO) is widely used as a cathode material in LIBs due to its excellent electrochemical properties. However, its capacity is limited by structural changes and severe side reactions at high voltage and temperature. To overcome this issue, this study combines two strategies to enhance the intercalation kinetics of the LCO cathode. First, ionic pillars of various ions (e.g.,  $\text{Mg}^{2+}$  and  $\text{Ca}^{2+}$ ) are doped to stabilize the structure at high voltage. Second, lithium-ion conducting lithium phosphate ( $\text{Li}_3\text{PO}_4$ ) is coated to prevent direct contact between the liquid electrolytes and LCO particles, minimizing the formation of resistive surface films. The combination of these strategies results in a synergetic effect that significantly improves the energy density, thermal stability, cycling stability, and rate capability of the cathode. A rate capability of  $100 \text{ mAh g}^{-1}$  at 10C is achieved, and a stable cycle performance with 98% capacity retention after 100 cycles at 0.5C is observed. Herein, the potential pathways of enhancing the energy density of current cathode materials through a synergistic combination of surface and structural engineering are highlighted.

## 1. Introduction

The challenges of reducing greenhouse gas emissions in transportation involve decreasing the reliance on fossil fuels and promoting the widespread use of electric vehicles (EVs). Lithium-ion battery (LIB) research encourages the growth and widespread adoption of EV technology, lowers the use of foreign oil, and limits the emission of greenhouse gases.<sup>[1–3]</sup> Therefore, the advancement of a power generation device with a minimal environmental impact has been a highly active area of research.<sup>[4,5]</sup> This has led to significant advancements in power-storage technology such as the fuel cell, redox flow batteries, metal-ion batteries, lithium–air batteries, etc. Lithium-ion secondary batteries are widely used in various portable devices such as mobile phones, smartphones, laptops, portable music players, digital cameras, and medical devices.<sup>[6]</sup> Additionally, lithium-ion secondary batteries can also


be utilized as a power source for EVs such as hybrid EVs (HEVs), EVs, and plug-in hybrid EVs (PHEVs), driving the adoption of clean energy as the next generation of transportation.<sup>[7–10]</sup> Current EVs face the major challenge of long charging times, which can range from 30 min to several hours. For electromobility to be competitive with internal combustion engines, fast charging is crucial. The goal is to be able to recharge 75%–80% of high-energy density cells within 10–15 min by 2023.<sup>[11,12]</sup> To overcome the interfacial and structural limitations of fast charging, it is imperative to find new lithium-ion intercalation materials with highly stable structures that can facilitate ultrafast lithium-ion diffusion and reversible electrochemical reactions.

Lithium cobalt oxide ( $\text{LiCoO}_2$  or LCO) has been widely used as a cathode for LIBs due to its high tap density, easily synthesizable process, and exceptional stability during cycling at 4.3 V.<sup>[13,14]</sup> The cathode materials, such as  $\text{LiCoO}_2$  (LCO),  $\text{LiMn}_2\text{O}_4$  (LMO),  $\text{LiFePO}_4$  (LFP),  $\text{LiNi}_{0.33}\text{Co}_{0.33}\text{Mn}_{0.33}\text{O}_2$  (NMC), and  $\text{LiNi}_{0.8}\text{Co}_{0.15}\text{Al}_{0.05}\text{O}_2$  (NCA), play a crucial role in determining the electrochemical performance of LIBs. Despite these advancements, these cathode materials still face limitations in terms of capacity, rate capability, and stability during high-voltage, fast-charging conditions. Despite significant progress since the introduction of the first commercial LCO batteries, LCO electrodes are

F. Hasan, H. D. Yoo  
Department of Chemistry and Chemical Institute for Functional Materials  
Pusan National University  
Busan 46241, Republic of Korea  
E-mail: hyundeog.yoo@pusan.ac.kr

F. Hasan, A. A. A. Abdelazeez  
Nanoscale Science  
Department of Chemistry  
The University of North Carolina at Charlotte  
Charlotte, NC 28223, USA  
E-mail: fhasan1@uncc.edu

M. Rabia  
Nanomaterials Science Research Laboratory  
Chemistry Department  
Faculty of Science  
Beni-Suef University  
Beni-Suef 62521, Egypt

 The ORCID identification number(s) for the author(s) of this article can be found under <https://doi.org/10.1002/ente.202300153>.

© 2023 The Authors. Energy Technology published by Wiley-VCH GmbH. This is an open access article under the terms of the Creative Commons Attribution License, which permits use, distribution and reproduction in any medium, provided the original work is properly cited.

DOI: 10.1002/ente.202300153

still not utilized at 4.5 V (vs. Li/Li<sup>+</sup>), which is readily available in the market.<sup>[15–18]</sup> To maximize the energy density of LCO, it is necessary to unlock the capacity limits of the cathode material by operating at a higher cutoff voltage. However, high-voltage operation of batteries can result in several challenges such as order–disorder transitions, reduced Li<sup>+</sup> diffusivity, critical stresses, electrolyte decomposition, and Co dissolution.<sup>[19,20]</sup> To address these issues, various approaches have been proposed to improve the cycle stability of LiCoO<sub>2</sub> at high voltage. Among the various strategies, doping with different elements is the most promising and effective in improving the electrochemical performance of LiCoO<sub>2</sub> while maintaining structural durability. This method involves the addition of various metal elements, such as Sr, Zr, Mg, Ca, La, and Al, to the cathode material of LIBs. This approach has been suggested as a successful way to enhance cycling stability.<sup>[21–23]</sup> Incorporating Mg<sup>2+</sup> into the LiO<sub>2</sub> layer can stabilize its structure. However, the addition of Mg dopants does not significantly impact the capacity enhancement of LiCoO<sub>2</sub>, as they serve only as a compensator for the Co<sup>4+</sup> charge.<sup>[24,25]</sup> Recent investigations aimed at addressing the performance issues of LiCoO<sub>2</sub> have used various approaches with promising results. For example, Liu et al. reported that doping with La and Al can greatly enhance the Li diffusivity and structural stability of LiCoO<sub>2</sub> during high-voltage operation. Similarly, Zhang et al. reported significant improvement in the cycle and rate performance of LiCoO<sub>2</sub> at a high-charging cutoff voltage of 4.6 V through Ti–Mg–Al co-doping with approximately 0.1 wt% of each dopant. These efforts to enhance the performance of LiCoO<sub>2</sub> have had varying degrees of success. Different techniques, such as coating LCO particles with oxides, phosphates, and other positive electrode materials have been explored.<sup>[26,27]</sup> In many cases, coatings have been found to improve the cycling and performance of LiCoO<sub>2</sub>, although not in all instances. Lithium-ion diffusion within the electrode determines the discharge process at different current densities, which is the rate-limiting step. It is believed that the successful incorporation of dopants into the LCO structure enables LCO to function at high-voltage cycling, thereby improving lithium-ion diffusivity. Generally, increasing the distance between the layers facilitates the solid-state diffusion of Li<sup>+</sup> in layered materials by reducing the energy required for Li<sup>+</sup> to move from one stable site to

another through the spaces between the layers.<sup>[28–34]</sup> In this study, we aimed to improve the structural stability and intrinsic Li<sup>+</sup> diffusivity of LiCoO<sub>2</sub> during battery operation through two strategies, first, by incorporating larger ions into the layered structure to enhance the stability. Second, using solid-state electrolyte Li<sub>3</sub>PO<sub>4</sub> as a coating material for both pristine (P–LCO) and doped LiCoO<sub>2</sub> (D–LCO) cathode is expected to improve the ionic conductivity at the interface between the active material electrolyte, thermal stability, and overall electrochemical performance. By utilizing a combined approach, we were able to achieve remarkable results, including a high rate capability of approximately 100 mAh g<sup>−1</sup> at 10C rate (6 min charge or discharge) and stable cycling performance of around 98%, 92.7% capacity retention after 100 cycles at a 0.5C, both at 25 and 60 °C. This combined strategy offers new insights into unlocking the full potential of current cathode materials in terms of energy density.

## 2. Result and Discussion

### 2.1. Topological Analysis of P–LCO and D–LCO Samples

The LCO powder samples were synthesized using a solid-state route and analyzed using XRD (Figure 1a). The results showed clear patterns of P–LCO and D–LCO, which are isostructural to layered NaFeO<sub>2</sub> with a R $\bar{3}$ m space group.<sup>[35–37]</sup> This confirms the successful synthesis of the samples without impurities. The XRD patterns display well-defined (0 0 3)–(0 0 6) and (1 0 1)–(1 1 3) peaks, indicating a dimensionally stable structure with an ordered distribution of cations in the lattice. The SEM photographs of the pristine and LiCo<sub>1–x</sub>M<sub>x</sub>O<sub>2</sub> (X = 0.02) powders showed well-crystallized particles with hexagonal shapes. The solid-state samples had an average particle size of 1.5–2 μm and were evenly distributed. However, through the process, due to controlled ball milling, the particle size was reduced, resulting in smaller particles.

In this study, the Rietveld refinement method, which is a least-squares refinement procedure, was utilized to calculate XRD patterns using the PDXL software from Rigaku. The XRD patterns were indexed as the αNaFeO<sub>2</sub> structure with a hexagonal lattice, based on the space group R $\bar{3}$ m. It was observed that all the

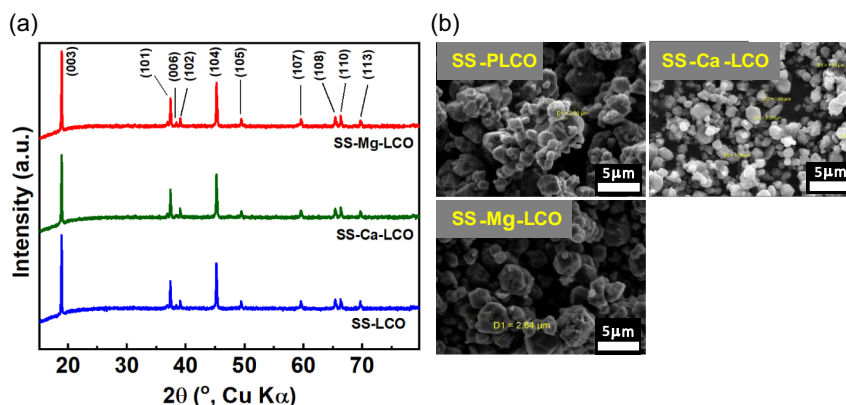


**Figure 1.** a) X-ray diffraction (XRD) spectra of pristine lithium cobalt oxide (LiCoO<sub>2</sub>, P–LCO) and doped LCO (D–LCO), and b) the scanning electron microscope (SEM) topographical image of P–LCO, D–LCO (scale bar equals 5 μm).

samples had a peak value ratio of  $I(003)/I(104)$  larger than 1.2, which is considered a measure of the cation-mixing degree. This suggests that cation mixing did not occur in any of the samples.<sup>[38,39]</sup>

The as-prepared samples exhibited  $c/a$  values around 4.989, which is higher than the value (4.899) observed in a cation-disordered rock salt structure.<sup>[40]</sup> This suggests that the parameters for the D-LCO samples have only slightly increased (as shown in Figure 2).

The energy-dispersive X-ray spectroscopy (EDX) spectra of  $\text{LiCo}_{1-x}\text{M}_x\text{O}_2$  (D-LCO) are shown in S1, Supporting Information. The spectra show the presence of other elements such as Ca, Mg, Co, and M (where M could be any element that is doped into the  $\text{LiCoO}_2$  structure). The presence of these elements can be seen from the peaks corresponding to their respective K-shell electrons. The intensities of these peaks can provide information about the relative amounts of the elements present in the sample.

The spectra of D-LCO reveal that the samples consist of Co, O, and doped elements. The EDX spectra of the respective compositions indicate the formation of stoichiometric controlled and homogeneous samples. The peaks are clearly identified as originating from the respective elements, with the most intense peak being that of Co, due to its significant presence in terms of weight.

High-angle annular dark-field STEM (HAADF STEM) mapping can provide high-resolution imaging of the distribution

of elements in a sample. The results we mentioned, showing a homogeneous distribution of Ca and Mg elements in the single crystal structure of Ca-LCO and Mg-LCO, indicate that the doping process was successful and the elements were well incorporated into the  $\text{LiCoO}_2$  structure. The presence of phosphorus (P) in the structure, as seen from the HAADF STEM mapping, is a clear indication of the presence of  $\text{Li}_3\text{PO}_4$  at the edges of the single particle. This suggests that the  $\text{Li}_3\text{PO}_4$  coating was successfully deposited onto the  $\text{LiCoO}_2$  particles, which can play a role in improving the stability and electrochemical performance of the material.

The HAADF STEM mapping results provide valuable information about the distribution and location of elements in the sample, which can help in understanding the structural and compositional changes that occur during the coating process. To further validate the effect of lithium phosphate ( $\text{Li}_3\text{PO}_4$ , LPO) modification on both pristine and doped samples and its relationship with performance, high-resolution TEM analyses were carried out on three different samples: LPO-LCO, LPO-Mg-LCO, and LPO-Ca-LCO. As depicted in Figure S2, Supporting Information, an amorphous layer can be observed on the surface of the samples with 2 wt% LPO content. It should be noted, however, that the thickness of the amorphous layer increases with higher wt% of LPO, for instance, 5%, which could lead to significant lattice distortion during long-term cycling. This, in turn, may result in poor ion-transport dynamics and inferior cycle retention, as has been reported in several studies. Therefore, the electrochemical performance of LCO modified with a moderate LPO content is better Figure 3.

## 2.2. Electrochemical Performances

$\text{LiCoO}_2$  is a commonly used cathode material in LIBs due to its stability at 4.3 V. This stability is related to the LCO crystal structure and how  $\text{Li}^+$  moves in and out into the cathode material during charging and discharging. In LIBs, the cathode is charged to a high voltage during charging and discharged to a lower voltage during use. LCO has a unique crystal structure that allows for the orderly insertion and removal of lithium ions, which helps to maintain the voltage stability of the cathode. Up to 4.3 V, the cathode maintains a balance between the energy stored in the lithium ions and the energy required to maintain the crystal structure. This stability is crucial for ensuring the long-term performance and safety of the battery. The stability of the LCO cathode refers to its ability to maintain its performance over multiple charge-discharge cycles. In Figure 4a,b, the LCO cathode is shown to be stable up to 50 cycles, meaning that its performance remains consistent throughout this period of use. Compared to calcium (Ca) and magnesium (Mg) D-LCO, the undoped LCO cathode has a higher stability due to its more homogeneous structure and fewer impurities. Ca and Mg doping can lead to changes in the crystal structure of LCO although, at high voltage (4.5 V), rate and temperature cathodes performances are significantly different.

The experiments were conducted on bare LCO and D-LCO with  $\text{Mg}^{2+}$  and  $\text{Ca}^{2+}$  on purpose to evaluate their electrochemical performance. The doping process was done using a solid-state doping method, which has been shown to result in better

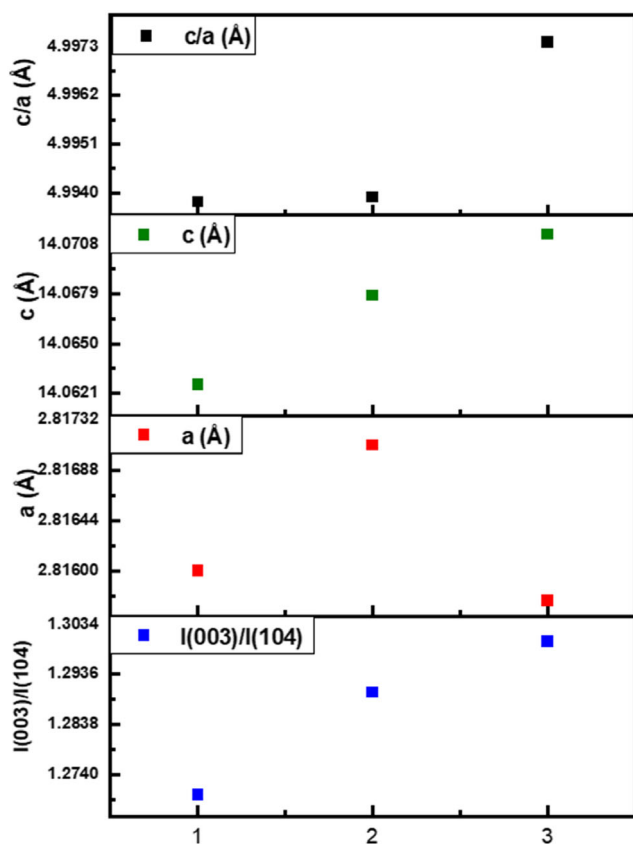


**Figure 2.** Rietveld refinement study of P-LCO and doped samples.

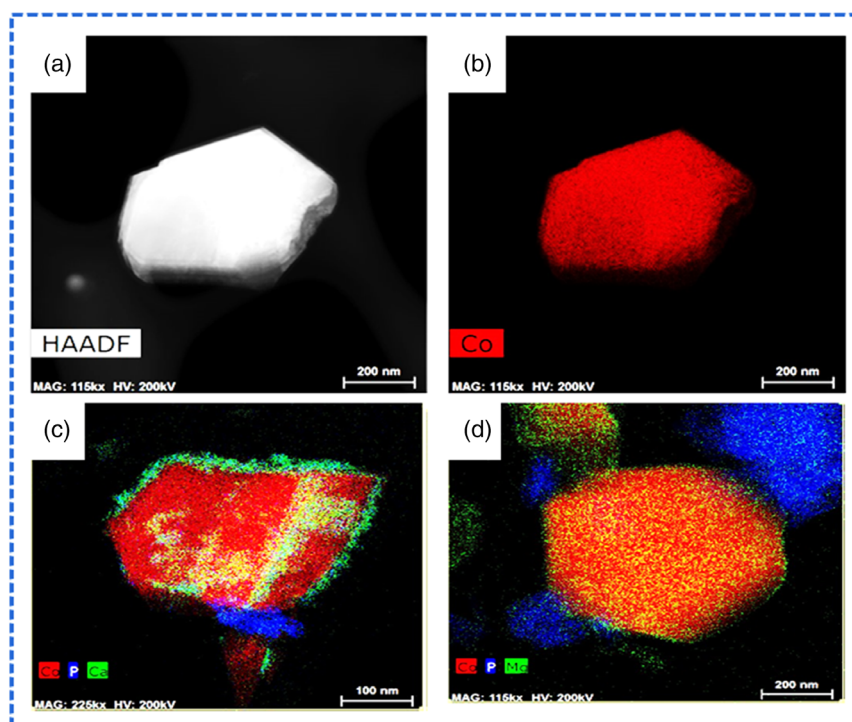


**Figure 3.** a–d) High-angle annular dark field-Scanning transmission electron microscopy (HAADF-STEM) images along with the color-coded elemental maps for lithium phosphate ( $\text{Li}_3\text{PO}_4$ , LPO)-coated Ca-LCO and Mg-LCO.

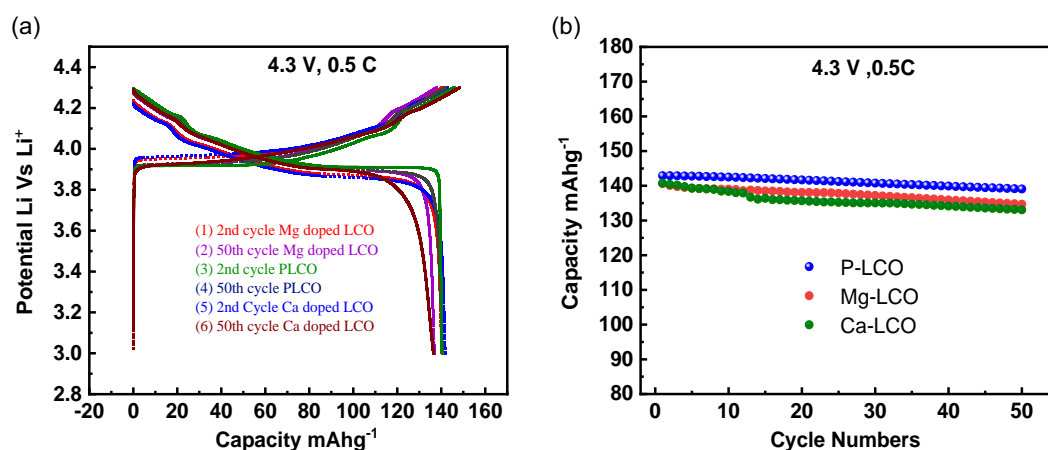


**Figure 4.** a,b) Galvanostatic charge-discharge (GCD) profile shows the cyclic performance at 25 °C operated at 4.3 V, 0.5C.

electrochemical performance according to previous studies from the authors' research group. The intent of the doping is to increase the interlayer distance in LCO, which can act as an ionic pillar and allow for faster and freer  $\text{Li}^+$  diffusion during the charge-storage process. The results of the Rietveld refinement show that  $c$  parameters increased, which indicate that the interlayer distance has increased in the doped samples compared to the bare LCO, demonstrating that the interlayer distance has indeed been expanded.<sup>[41,42]</sup> The expanded interlayer distance is crucial for efficient electrochemical performance as it reduces the shared faces between the  $\text{Li}^+$  and  $\text{Co}^{3+/4+}$  ions, allowing for a

greater distance between the two, which significantly improves the charging and discharging process. Overall, the results suggest that the D-LCO samples produced in this study are more favorable for use in LIBs due to their increased interlayer distance and improved electrochemical performance.<sup>[43,44]</sup>

The results of the half-cell tests at operating temperature 25 and 60 °C indicate that the selective ion-doped D-LCO sample outperforms the P-LCO cathode in terms of specific capacity and thermal stability. The higher specific capacity of D-LCO ( $120\text{--}151\text{ mAh g}^{-1}$ ) compared to P-LCO ( $80\text{ mAh g}^{-1}$ ) at 0.5C rate suggests that the doping process was successful in



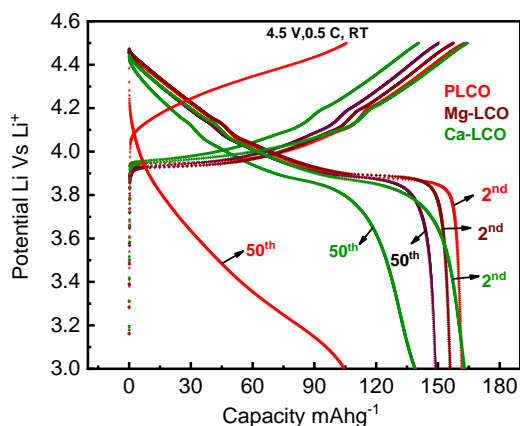


**Figure 5.** GCD profile shows the cyclic performance at 25 °C operated at 4.5 V, 0.5C.

improving the  $\text{Li}^+$ -storage capabilities of  $\text{LiCoO}_2$  at room temperature. As shown in **Figure 5**, the charge–discharge profiles of the P-LCO and the D-LCO were compared and the results showed that the P-LCO experienced more severe polarization in the first 50 cycles. This suggests the P-LCO exposure to significant structural degradation during the charging and discharging processes.

As mentioned earlier, deep charging can cause the oxidation of  $\text{Co}^{2+}$  to  $\text{Co}^{4+}$ , leading to corrosion of the LCO surface and destroying its cathode crystallinity. This is due to the reaction between the oxidized  $\text{Co}^{4+}$  and the liquid electrolyte.<sup>[45,46]</sup> However, this destructive process is prevented in the LPO-LCO samples due to the presence of a discrete LPO protective layer. This layer acts as a barrier, preventing the corrosive reaction from taking place and preserving the LCO's structural integrity which is shown strategy (2) at our work.

The performance of the D-LCO cathode even after 100 cycles indicates its excellent cyclic stability, which is critical for the long-term reliability of a battery. The ability of the D-LCO cathode to retain its high specific capacity at elevated temperature (60 °C)

demonstrates its thermal stability and its potential for use in high-temperature regions. As shown in **Figure 6**, the cells that were operated at 60 °C showed a higher percentage of their initial capacity than the battery operated at 25 °C. This suggests that the thermo-electrochemical structural reconstruction or surface stabilization occurred during the initial formation cycling at higher temperature. We believe that this process works by using the heat to accelerate the chemical reactions within the cell, causing a faster and more thorough structural rearrangement. As a result, the cathode's surface becomes more stable and resistant to degradation over time, leading to a higher retention of the initial capacity even after multiple cycles. Therefore, operating the cells at 60 °C during the initial formation cycling helps to improve the stability of the cathode and prolong the battery's overall lifespan.

As strategy (2), the authors coated P-LCO and D-LCO with a thin layer of LPO ( $\text{Li}_3\text{PO}_4$ ) to protect the LCO structure from attack by hydrogen fluoride (HF) produced by the decomposition of lithium salt-containing electrolytes. According to theory, a thin LPO coating layer can act as a barrier and prevent the HF from reaching the LCO structure and causing damage. The surface morphology of both the pristine and LPO-coated D-LCO powders was analyzed to understand the effects of the LPO coating on the structure of the cathode. By studying the surface morphologies of the two materials, the authors were able to determine the effectiveness of the LPO coating in protecting the LCO structure from the damage caused by HF. The use of LPO coating on P-LCO and D-LCO is pivotal for improving the stability and durability of the cathode in LIBs. By preventing the attack of HF, the LPO coating helps to maintain the structural integrity of the cathode and prolong the overall lifespan of the battery. A general schematic diagram and coating process are depicted in **Figure 7**.

The LPO coating on the D-LCO cathodes helps to reduce the overpotential, which is the extra energy required to drive the reaction, and leads to better electrochemical performance. This is because LPO is an electronic conductor, meaning it allows the electrons to flow freely and efficiently through the cathode.

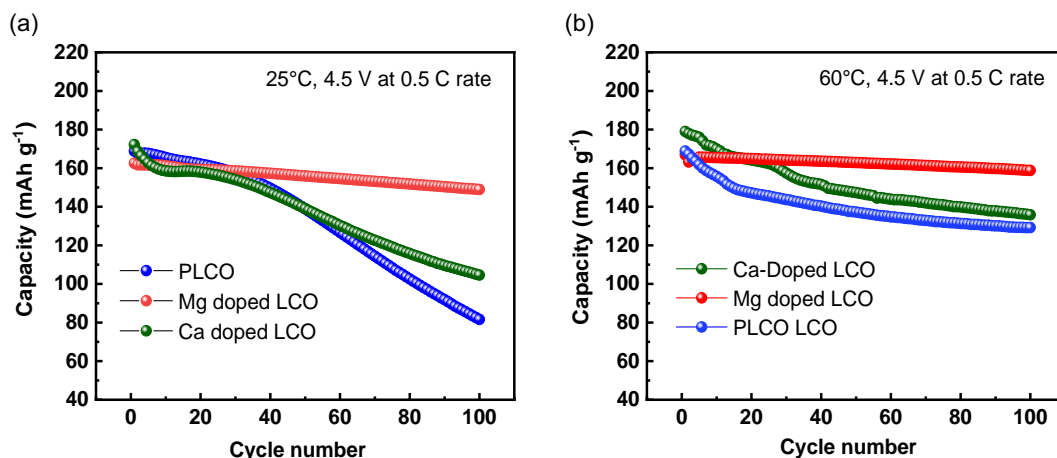


**Figure 6.** a, b) Cyclic stability analysis based on capacity retention of PLCO, DLCO, LPO coated samples Barchart-1, 25°, BarChart-2, 60° after 100 cycles at 4.5-V, 0.5-C.

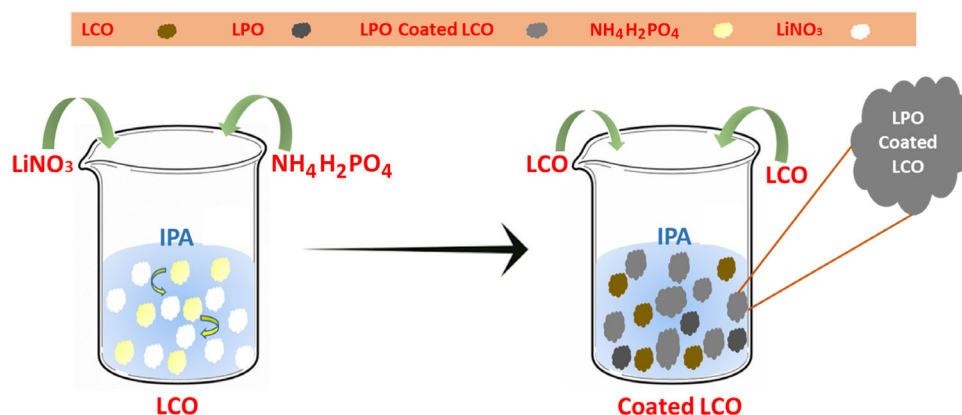


**Figure 7.** Schematic diagram of  $\text{Li}_3\text{PO}_4$  (LPO)-coating process on P-LCO and D-LCO cathode.

The LPO coating on the D-LCO cathode helps to improve the stability of the cathode, resulting in better cyclic stability, meaning the capacity of the cathode remains consistent even after repeated charge and discharge cycles. The LPO-coated D-LCO cathode with Mg (magnesium) showed the highest capacity retention after 100 cycles both at room temperature and elevated temperature as shown in **Figure 8a,b**. This is due to the electronic conductivity of the LPO coating, as well as the catalytic properties of Mg, which help to enhance the reaction kinetics and improve the overall performance of the cathode.

Based on the data in bar chart 1, the cycle performance comparison of various electrodes was performed at 4.5 V, 0.5C. The first cycle capacity and the 100th cycle capacity of three samples (P-LCO, Ca-LCO, and Mg-LCO) were recorded at both 25 and 60 °C. At 25 °C, P-LCO had a first cycle capacity of 168.80  $\text{mAh g}^{-1}$  and 100th cycle capacity of 81.63  $\text{mAh g}^{-1}$ , resulting in a capacity loss of 87.17  $\text{mAh g}^{-1}$ . Ca-LCO had a first cycle capacity of 172.20  $\text{mAh g}^{-1}$  and a 100th cycle capacity of 104.25  $\text{mAh g}^{-1}$ , resulting in a capacity loss of 67.95  $\text{mAh g}^{-1}$ . Meanwhile, Mg-LCO had a first cycle capacity of 166.91  $\text{mAh g}^{-1}$  and a 100th cycle capacity of 158.78  $\text{mAh g}^{-1}$ , resulting in a capacity loss of only 8.13  $\text{mAh g}^{-1}$ , as shown in **Figure 9** and Table 2, Supporting Information.

At 60 °C, P-LCO had a first cycle capacity of 179.0  $\text{mAh g}^{-1}$  and a 100th cycle capacity of 135.45  $\text{mAh g}^{-1}$ , resulting in a capacity loss of 43.55  $\text{mAh g}^{-1}$ . Ca-LCO had a first cycle capacity of 170.01  $\text{mAh g}^{-1}$  and 100th cycle capacity of 129.07  $\text{mAh g}^{-1}$ , resulting in a capacity loss of 40.94  $\text{mAh g}^{-1}$ . Mg-LCO had a first cycle capacity of 166.9  $\text{mAh g}^{-1}$  and a 100th cycle capacity of 157.8  $\text{mAh g}^{-1}$ , resulting in a capacity loss of 9.1  $\text{mAh g}^{-1}$ . The results indicate that Mg-LCO has the best cycle performance compared to P-LCO and Ca-LCO, with the lowest capacity loss in both 25 and 60 °C conditions.

Based on the data in bar chart 2, half cycle performance comparison of various electrodes was performed at 4.5 V and 0.5C, with the capacity measured at both 25 and 60 °C. For LPO-P-LCO, the first cycle capacity at 25 °C was 154.38  $\text{mAh g}^{-1}$ , and the 100th cycle capacity was 112.26  $\text{mAh g}^{-1}$ , resulting in a capacity loss of 42.11  $\text{mAh g}^{-1}$ . At 60 °C, the first cycle capacity was 175.56  $\text{mAh g}^{-1}$ , and the 100th cycle capacity was 146.63  $\text{mAh g}^{-1}$ , resulting in a capacity loss of 28.93  $\text{mAh g}^{-1}$ . This indicates that LPO-P-LCO has a relatively high capacity loss at both 25 and 60 °C, which may affect the battery performance upon further cycling.

For LPO-Ca-LCO, the first cycle capacity at 25 °C was 169.89  $\text{mAh g}^{-1}$ , and the 100th cycle capacity was

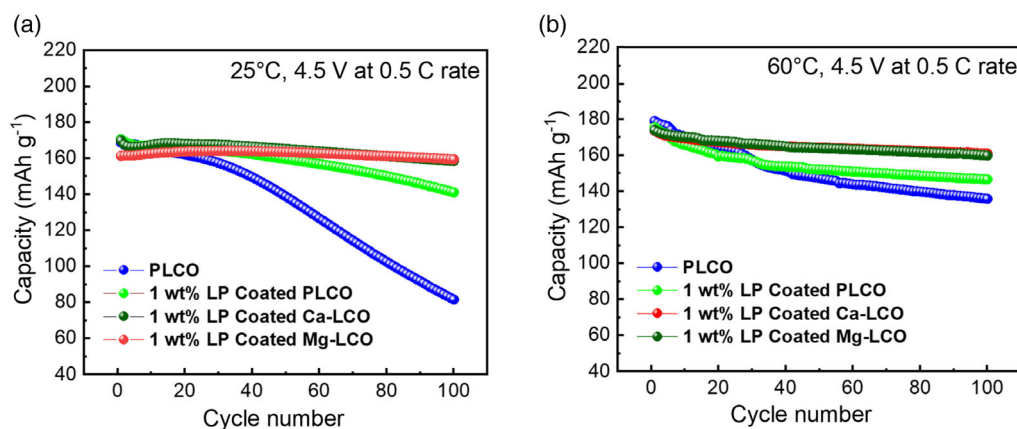


**Figure 8.** a,b) GCD cycle capability study and thermal stability test of P-LCO and coated P-LCO, D-LCO half-cells studied at 25 and 60 °C.

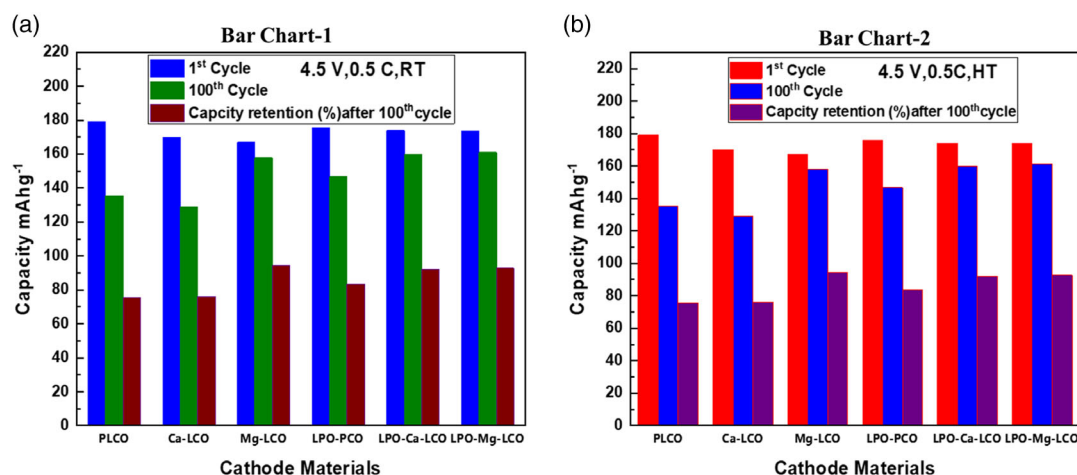


**Figure 9.** a,b) Cyclic stability analysis based on capacity retention of PLCO, DLCO, LPO Coated samples BarChart-1, 25°, BarChart-2, 60° after 100 cycles at 4.5 V, 0.5 C.

158.54 mAh g<sup>-1</sup>, resulting in a capacity loss of 11.35 mAh g<sup>-1</sup>. At 60 °C, the first cycle capacity was 173.89 mAh g<sup>-1</sup>, and the 100th cycle capacity was 159.79 mAh g<sup>-1</sup>, resulting in a capacity loss of 14.1 mAh g<sup>-1</sup>. This indicates that LPO–Ca–LCO has a lower capacity loss than LPO–P–LCO, but still relatively high compared to LPO–Mg–LCO. For LPO–Mg–LCO, the first cycle capacity at 25 °C was 161.37 mAh g<sup>-1</sup>, and the 100th cycle capacity was 159.49 mAh g<sup>-1</sup>, resulting in a capacity loss of only 1.88 mAh g<sup>-1</sup>. At 60 °C, the first cycle capacity was 173.61 mAh g<sup>-1</sup>, and the 100th cycle capacity was 161.04 mAh g<sup>-1</sup>, resulting in a capacity loss of 12.57 mAh g<sup>-1</sup>. This indicates that LPO–Mg–LCO has excellent cyclic stability, with lowest capacity loss at 25 and 60 °C.

Therefore, the LPO–Mg–LCO electrode has the best cycle performance compared to LPO–P–LCO and LPO–Ca–LCO, with a low capacity loss of 1.88 mAh g<sup>-1</sup> at 25 °C and 12.57 mAh g<sup>-1</sup> at 60 °C after 100 cycles. This suggests that LPO–Mg–LCO may be the best choice for battery applications where high cycle stability and low capacity loss is required, regardless of temperature among all samples.

The differential capacity dQ/dV plots provide valuable insight into the performance of cathodes in LIBs. The differential capacity plots are pivotal in determining the capacity retention and potential-dependent fading mechanisms in the electrodes during cycling. The dQ/dV plots reflect the potential-related capacity degradation and provide information on the potential hysteresis that occurs in the voltage profiles during high-voltage cycling. These graphs are crucial in understanding the changes in the active material phases and the impact of overpotential on the performance of the cathode. The dQ/dV plots can help identify the root causes of capacity fading and provide valuable information for improving the overall performance and cycle stability of LIBs. The dQ/dV plots in Figure 10a,c,d indicates potential-related capacity degradation, resulting in potential hysteresis in voltage profiles after 10 cycles and 60 cycles. dQ/dV plots for the samples are crucial indicators for determining phase retention during cycling. The P–LCO electrodes show a decrease in peak capacity after 60 cycles due to the degradation mechanisms caused by impedance growth Figure 12. The clear separation of cathodic

peaks at around 3.8–4.0 V in the Mg-doped materials is probably due to the faster electrochemical kinetics of these samples at the 10th cycle. In contrast, the voltage difference between the anodic and cathodic peaks is lowest in the Mg–D–LCO coated with LPO solid-state electrolyte, demonstrating that this material has the lowest overpotential and best kinetics, even after the 60th cycle. The LPO-coated D–LCO maintained its main peak at 3.85 V versus Li/Li<sup>+</sup> during high-voltage cycling, while the P–LCO lost most of its main peaks due to more severe side reactions on the surface. These results highlight that optimized LPO-coating can enhance the rate and cycle performance of D–LCO cathodes by protecting the surface from side reactions, resulting in reduced interfacial resistance. At elevated temperatures, such as 60 °C, HF formation is accelerated and leads to cracking on the surface of the active materials. Although the LPO-coated D–LCO showed a larger capacity than the P–LCO by 20–30 mAh g<sup>-1</sup> at 60 °C (Figure 10), the capacity retention was similar for both pristine and coated samples. This suggests that raising the temperature to 60 °C results in a different capacity fading mechanism that requires an additional solution beyond surface protection by Li<sub>3</sub>PO<sub>4</sub>.

The rate capability of LIBs plays a critical role in their practical applications. To meet the fast-changing needs of modern devices, the rate capability of the battery must be high. The ability of a battery to maintain its capacity while being charged at a high rate is a crucial performance indicator. This study investigated the rate capability of D–LCO coated with LPO, as shown in Figure 11.

The rate capability test and specific capacity with the number of every 5 cycles at different C-rates (0.05C, 0.1C, 0.2C, 0.5C, 1C, 2C, 5C, 10C, and 0.05C) were evaluated. The relative capacity graph of LPO@D–LCO and doped samples were plotted. Relative capacity graphs for rate capability of LIBs display the relationship between the discharge capacity and the charging/discharging rate of an LIB. The graph is plotted with the charging/discharging rate on the x-axis and the relative capacity on the y-axis. The relative capacity is calculated as the ratio of the discharge capacity to the initial capacity of the battery.

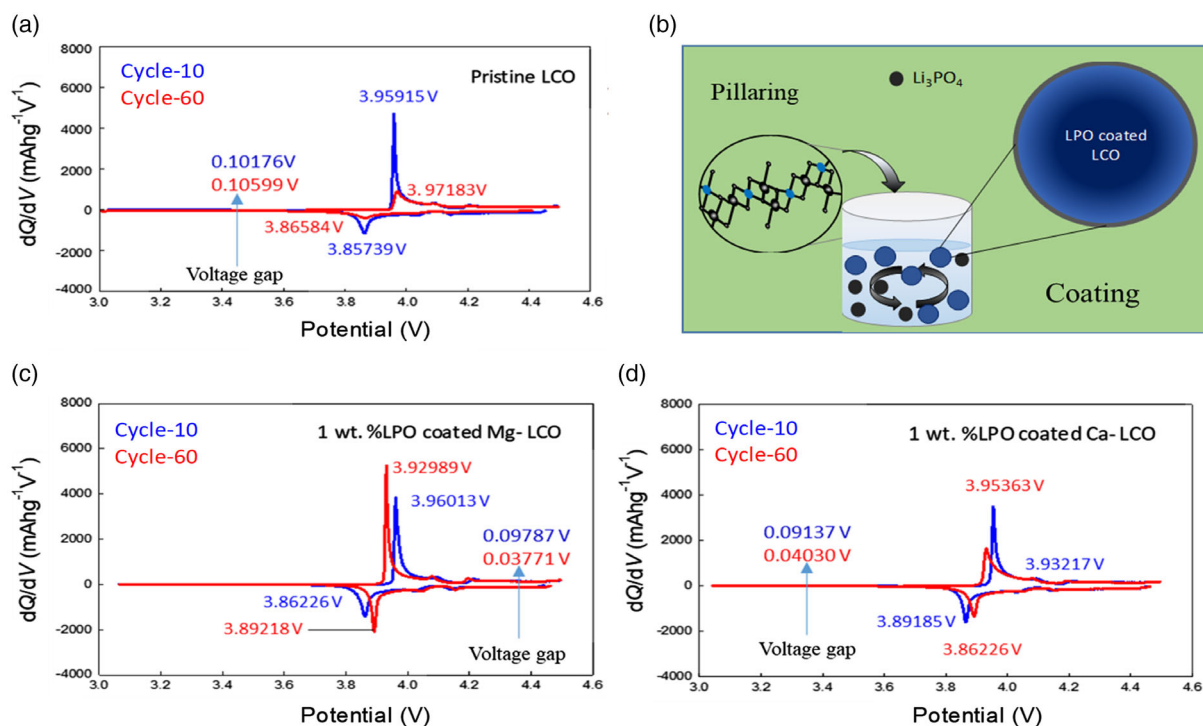


**Figure 10.** a,c,d) Corresponding  $dQ/dV$  plots of a Li/LCO (pristine and coated) standard lithium-ion half cells after 10 and 60 cycles between 3.0 and 4.5 V, and b) schematic approach to prevent the voltage drop during cycling.

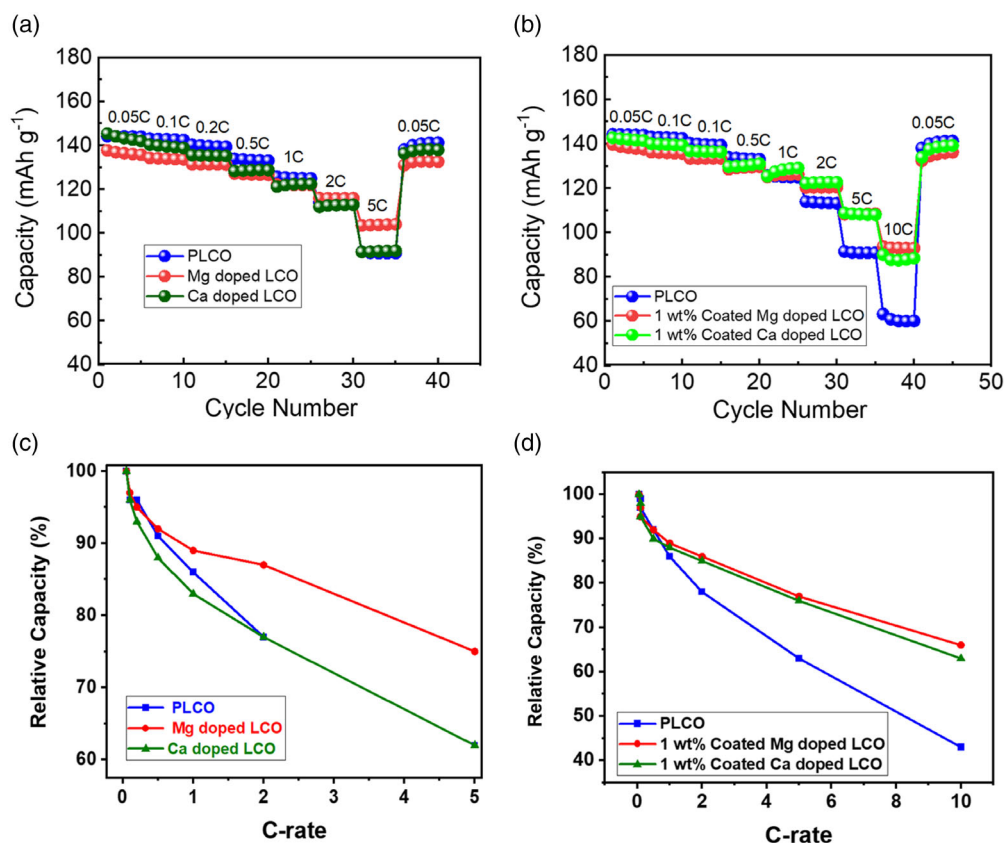


**Figure 11.** a,b) Typical rate capability test and the specific capacity with the number of every 5 cycles at different C-rate (0.05C, 0.1C, 0.2C, 0.5C, 1C, 2C, 5C, 10C, 0.05C); c,d) relative capacity (%) graph of coated and doped samples.



In a relative capacity graph, the higher the relative capacity, the better the rate capability of the battery. The shape of the graph can provide insight into the battery's performance and behavior at different C-rates. For example, a graph with a steep slope at high C-rates indicates that the battery's rate capability is better, meaning it can be operated with more current when required.

The results showed that the Mg–D-LCO with LPO coating secured 54% of its capacity at 5C rate, which was significantly better than the P-LCO. This demonstrates that the  $\text{Mg}^{2+}$  pillars provide stability to the layer-to-layer structure, allowing for  $\text{Li}^+$  to move back and forth with deftness. This is because the  $\text{Mg}^{2+}$  ion is believed to increase the activation energy for  $\text{Li}^+$  motion, which is related to the space between the oxygen layers in the cathode. By increasing this activation energy, the Mg–LCO cathode is able to retain its capacity better during high-rate charging. In contrast, the addition of  $\text{Ca}^{2+}$  showed only a slight improvement in terms of capacity retention compared to the P-LCO.

The study on the effect of LPO coating on the rate capability of D-LCO cathodes has shown promising results as well. The optimization of LPO coating has significantly improved the electrochemical performance of D-LCO cathodes. The results show that the Mg-pillared LCO with LPO coating secured 56% capacity at a 10C rate, whereas the P-LCO had limited retention. This means that the Mg–LCO with LPO coating can charge to  $100 \text{ mAh g}^{-1}$  specific capacity within just 6 min of charging at a 10C rate. This promising cycle stability and rate capability data also supported by our electrochemical impedance analysis of the representative samples. The Nyquist plot provides valuable information about the change in internal resistance of the battery during cycling, which can help readers better understand the performance of the battery over time. We compare the surface film resistance ( $R_f$ ) and charge-transfer resistance ( $R_{ct}$ ) of P-LCO and LPO-coated doped samples after 100 cycles at room temperature. The all-impedance plots illustrated in Figure 12 offer a visual representation of the variations among the different samples. In electrochemical systems, Nyquist plots typically show an oblique line in the low-frequency region and a semicircle in

the high-frequency region. The semicircle is indicative of the surface film and  $R_{ct}$ , which is considerably lower in coated doped samples.

In contrast, the oblique line corresponds to the Warburg impedance ( $Z_w$ ), which measures Li-ion diffusion within the particles.

The LPO coating acts as a protective layer, minimizing side reactions which can be detrimental to battery cells. The solid electrolyte coating on the surface of the secondary particle increases the ionic conductivity and acts as a fast channel for lithium-ion transport. This results in reduced interfacial resistance and improved rate capability, thermal stability, and cycle performance of LPO@D-LCO. Our results are compared with recently reported literature on 4.5 V, LCO (Table S3, Supporting Information).

### 3. Conclusion

The combination of ion pillaring and  $\text{Li}_3\text{PO}_4$ -coating strategies resulted in a highly improved energy density, rate performance, and cycling stability of the LCO cathode. The  $\text{Mg}^{2+}$ -pillared and  $\text{Li}_3\text{PO}_4$ -coated LCO showed remarkable electrochemical performance with a high initial specific capacity of  $175\text{--}180 \text{ mAh g}^{-1}$ , excellent rate capability, and stable cycling stability of 98%, 92% capacity retention after 100 cycles at 0.5C, 4.5 V at 25, 60 °C, respectively. The results of this study offer a promising approach toward fully exploiting the energy density of current cathode materials in LIBs for modern energy-storage applications. The combination of ion-pillaring and surface engineering techniques has proven to be a powerful tool for the development of next-generation cathode materials with improved electrochemical performance.

### 4. Experimental Section

**Solid-State Synthesis of P-LCO and D-LCO:** The process of preparing P-LCO and D-LCO involved mixing the precursors ( $\text{Li}_2\text{CO}_3$ ,  $\text{Co}_3\text{O}_4$ , and  $\text{Mg}(\text{NO}_3)_2 \cdot 6\text{H}_2\text{O}$  or  $\text{Ca}(\text{NO}_3)_2 \cdot 4\text{H}_2\text{O}$  as the dopant source) in the right proportions using a ball mill to achieve fine grinding. The mixture then calcined at 800 °C for 12 h, cooled down naturally, and ground before being finally sintered at 850 °C for 24 h in an air atmosphere. The precursor material of 10 g was used in this cost-effective and simple mechanochemical method.

**Coating Process on D-LCO:** Before the coating process, the D-LCO was synthesized through a solid-state reaction as described. The necessary stoichiometric amounts of  $\text{LiNO}_3$  and  $\text{NH}_4\text{H}_2\text{PO}_4$  were dissolved in 50 mL of isopropyl alcohol (IPA) as shown in Figure 6 in a separate container. The solutions were mixed thoroughly via sonication. Then, the doped or P-LCO powder was added to the mixed solution of coating agents, the solution was stirred overnight, and then filtered to collect the mixed powder. The resulting powder was dried in a vacuum oven for 12 h. After drying, the powder was ground and mixed using an agate mortar and pestle. Finally, the collected powder was taken to heat treatment at 300 °C for 5 h.

**Materials Characterization:** X-ray diffraction (XRD) was utilized using a MiniFlex 600 instrument from Rigaku Co., Japan, to analyze the elemental composition and crystal structure. The XRD analysis was carried out over a range of  $10\text{--}80^\circ$  ( $2\theta$ ) with a scanning speed of  $10 \text{ min}^{-1}$  and a slit width of 0.02. The surface topography of the synthesized samples was investigated using a VEGA3 scanning electron microscope (SEM) from Tescan Co. Physical and chemical properties of the layered P-LCO and D-LCO samples, including scanning transmission electron microscopy (STEM)

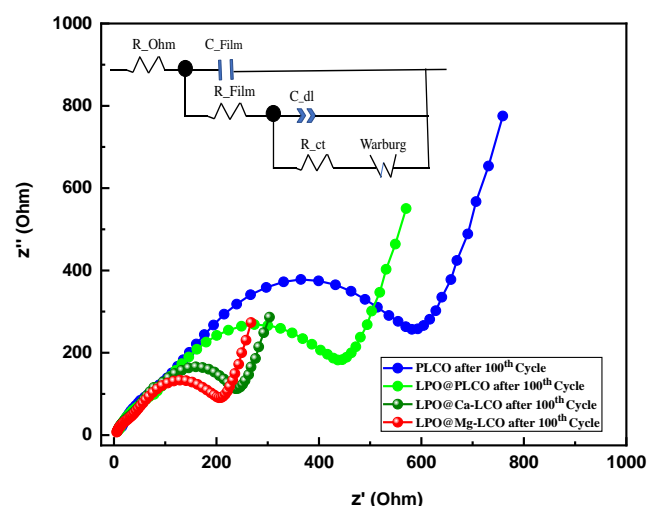


**Figure 12.** Nyquist plots of the Li||LCO cells measured at discharged state of 4.5 V after 100 cycles. The equivalent circuit used for spectra fitting is inset.

analysis and elemental mapping, were characterized using a JEOL JEM-F200 field-emission transmission electron microscope (FETEM) in Tokyo, Japan.

**Electrochemical Characterization:** To fabricate the electrodes, a mixture of N-methyl-2-pyrrolidone, P-LCO, conductive carbon black (Super-P), and polyvinylidene fluoride was applied onto an aluminum foil using a doctor blade in a ratio of 8:1:1. The mixture was then dried at 80 °C under vacuum for 2 h, after which it was rolled and punched into circular shapes with a diameter of 0.95 cm<sup>2</sup> and an active material loading of 1–2 mg. For the assembly of the 2032-type coin cells, these electrodes were used as the cathode, while a lithium foil was used as the anode, and a separator soaked in an electrolyte solution of 1 M lithium hexafluorophosphate in ethylene carbonate and ethyl methyl carbonate (EC: EMC, 3:7 w/w) was placed between them. The entire assembly process was carried out in a glove box that maintained a low level of moisture and oxygen below 1 ppm to ensure optimal conditions.

## Supporting Information

Supporting Information is available from the Wiley Online Library or from the author.

## Acknowledgements

This work was supported by the National Research Foundation (NRF) of the Korean Ministry of Science and MSIT (NRF-2021R1C1C1005446 and NRF-2018R1A5A1025594) and the nanoscale science Ph.D. Program at The University of North Carolina at Charlotte, U.S.A. The authors thank Jong Hun Sung for the fruitful discussion on the coating process of the cathode materials.

## Conflict of Interest

The authors declare no conflict of interest.

## Data Availability Statement

The data that supports the findings of this study are available in the supplementary material of this article.

## Keywords

capacity retention, coating, ion pillaring, lithium cobalt oxide

Received: February 15, 2023

Revised: March 24, 2023

Published online: May 1, 2023

- [1] D. Larcher, J.-M. Tarascon, *Nat. Chem.* **2015**, *7*, 19.
- [2] Y. Liu, Y. Zhu, Y. Cui, *Nat. Energy* **2019**, *4*, 540.
- [3] J. B. Dunn, L. Gaines, J. C. Kelly, C. James, K. G. Gallagher, *Energy Environ. Sci.* **2015**, *8*, 158.
- [4] H. Mostafa, A. M. Ahmed, M. Shaban, A. A. Abdel-Khaliek, F. Hasan, F. Mohammed Alzahrani, M. Rabia, *Photonics, Multidisciplinary Digital Publishing Institute, Basel, Switzerland* **2022**.
- [5] A. A. Abdelazeez, A. B. G. Trabelsi, F. H. Alkallas, M. Rabia, *Sol. Energy* **2022**, *248*, 251.
- [6] D. Deng, *Energy Sci. Eng.* **2015**, *3*, 385.
- [7] G.-L. Zhu, C. Z. Zhao, J. Q. Huang, C. He, J. Zhang, S. Chen, L. Xu, H. Yuan, Q. Zhang, *Small* **2019**, *15*, 1805389.

- [8] A. Masias, J. Marcicki, W. A. Paxton, *ACS Energy Lett.* **2021**, *6*, 621.
- [9] M. Li, M. Feng, D. Luo, Z. Chen, *Cell Rep. Phys. Sci.* **2020**, *1*, 100212.
- [10] S. Ahmed, I. Bloom, A. N. Jansen, T. Tanim, E. J. Dufek, A. Pesaran, A. Burnham, R. B. Carlson, F. Dias, K. Hardy, M. Keyser, *J. Power Sources* **2017**, *367*, 250.
- [11] J. Janek, W. G. Zeier, *Nat. Energy* **2016**, *1*, 1.
- [12] Y. Tang, Y. Zhang, W. Li, B. Ma, X. Chen, *Chem. Soc. Rev.* **2015**, *44*, 5926.
- [13] S. Choi, G. Wang, *Adv. Mater. Technol.* **2018**, *3*, 1700376.
- [14] J. Qian, L. Liu, J. Yang, S. Li, X. Wang, H. L. Zhuang, Y. Lu, *Nat. Commun.* **2018**, *9*, 1.
- [15] L. Wang, J. Ma, C. Wang, X. Yu, R. Liu, F. Jiang, X. Sun, A. Du, X. Zhou, G. Cui, *Adv. Sci.* **2019**, *6*, 1900355.
- [16] S. Kalluri, M. Yoon, M. Jo, S. Park, S. Myeong, J. Kim, S. X. Dou, Z. Guo, J. Cho, *Adv. Mater.* **2017**, *7*, 1601507.
- [17] T.-F. Yi, J. Mei, Y.-R. Zhu, *J. Power Sources* **2016**, *316*, 85.
- [18] Q. Liu, X. Su, D. Lei, Y. Qin, J. Wen, F. Guo, Y. A. Wu, Y. Rong, R. Kou, X. Xiao, F. Aguesse, *Nat. Energy* **2018**, *3*, 936.
- [19] H. Adenusi, G. A. Chass, S. Passerini, K. V. Tian, G. Chen, *Adv. Mater.* **2023**, *13*, 2203307.
- [20] J. H. Sung, F. Hasan, H. D. Yoo, *J. Korean Electrochem. Soc.* **2020**, *23*, 57.
- [21] S. Song, Y. Li, K. Yang, Z. Chen, J. Liu, R. Qi, Z. Li, C. Zuo, W. Zhao, N. Yang, M. Zhang, *J. Mater. Chem. A* **2021**, *9*, 5702.
- [22] J.-N. Zhang, Q. Li, C. Ouyang, X. Yu, M. Ge, X. Huang, E. Hu, C. Ma, S. Li, R. Xiao, W. Yang, *Nat. Energy* **2019**, *4*, 594.
- [23] F. Hasan, J. Kim, H. Song, S. H. Lee, J. H. Sung, J. Kim, H. D. Yoo, *J. Electrochem. Sci. Technol.* **2020**, *11*, 352.
- [24] L. Xu, K. Wang, F. Gu, T. Li, Z. Wang, *Mater. Lett.* **2020**, *277*, 128407.
- [25] H. Takamoto, A. West, *J. Electrochem. Soc.* **1997**, *144*, 3164.
- [26] R. B. Gupta, A. Patel, X. G. Sun, M. P. Paranthaman, M. Mou, J. H. Mugumya, M. Jiang, M. L. Rasche, H. Lopez, R. B. Gupta, *J. Mater. Chem. A* **2023**, *11*, 3789.
- [27] J. H. Sung, T. W. Kim, H. K. Kang, S. Y. Choi, F. Hasan, S. K. Mohanty, J. Kim, M. K. Srinivasa, H. C. Shin, H. D. Yoo, *Korean J. Chem. Eng.* **2021**, *38*, 1059.
- [28] Y. Lyu, X. Wu, K. Wang, Z. Feng, T. Cheng, Y. Liu, M. Wang, R. Chen, L. Xu, J. Zhou, Y. Lu, *Adv. Mater.* **2021**, *11*, 2000982.
- [29] Q. Li, G. Li, C. Fu, D. Luo, J. Fan, L. Li, *ACS Appl. Mater. Interfaces* **2014**, *6*, 10330.
- [30] K. Kang, Y. S. Meng, J. Breger, C. P. Grey, G. Ceder, *Science* **2006**, *311*, 977.
- [31] A. Van der Ven, *Electrochem. Solid-State Lett.* **1999**, *3*, 301.
- [32] Q. Shi, R. Qi, X. Feng, J. Wang, Y. Li, Z. Yao, X. Wang, Q. Li, X. Lu, J. Zhang, Y. Zhao, *Nat. Commun.* **2022**, *13*, 3205.
- [33] Y. Wei, J. Zheng, S. Cui, X. Song, Y. Su, W. Deng, Z. Wu, X. Wang, W. Wang, M. Rao, Y. Lin, *J. Am. Chem. Soc.* **2015**, *137*, 8364.
- [34] Y. Wang, Z. Feng, P. Cui, W. Zhu, Y. Gong, M. A. Girard, G. Lajoie, J. Trottier, Q. Zhang, L. Gu, Y. Wang, *Nat. Commun.* **2021**, *12*, 13.
- [35] R. Berthelot, M. Pollet, J. P. Doumerc, C. Delmas, *Inorg. Chem.* **2011**, *50*, 6649.
- [36] D. Carlier, M. Blangero, M. Ménétrier, M. Pollet, J. P. Doumerc, C. Delmas, *Inorg. Chem.* **2009**, *48*, 7018.
- [37] D. Carlier, I. Saadoun, M. Ménétrier, C. Delmas, *J. Electrochem. Soc.* **2002**, *149*, A1310.
- [38] T. Weigel, F. Schipper, E. M. Erickson, F. A. Susai, B. Markovsky, D. Aurbach, *ACS Energy Lett.* **2019**, *4*, 508.
- [39] X. Zhu, K. Shang, X. Jiang, X. Ai, H. Yang, Y. Cao, *Ceram. Int.* **2014**, *40*, 11245.

- [40] S. Madhavi, G. S. Rao, B. V. R. Chowdari, S. F. Y. Li, *J. Electrochem. Soc.* **2001**, *148*, A1279.
- [41] S. Levasseur, M. Ménétrier, C. Delmas, *Chem. Mater.* **2002**, *14*, 3584.
- [42] Y. S. Meng, M. E. Arroyo-de Dompablo, *Energy Environ. Sci.* **2009**, *2*, 589.
- [43] K. Kang, G. Ceder, *Phys. Rev. B* **2006**, *74*, 094105.
- [44] K.-H. Chen, M. J. Namkoong, V. Goel, C. Yang, S. Kazemiabnavi, S. M. Mortuza, E. Kazyak, J. Mazumder, K. Thornton, J. Sakamoto, N. P. Dasgupta, *J. Power Sources* **2020**, *471*, 228475.
- [45] H. Yuan, W. Song, M. Wang, Y. Gu, Y. Chen, *J. Alloys Compd.* **2019**, *784*, 1311.
- [46] L. Yang, K. Yang, J. Zheng, K. Xu, K. Amine, F. Pan, *Chem. Soc. Rev.* **2020**, *49*, 4667.